Orientation Bias of Optically Selected Galaxy Clusters and its Impact on Stacked Weak Lensing Analyses

Jörg P. Dietrich[*,1,2,3], Yuanyuan Zhang[3], Jeeseon Song[3], Christopher P. Davis[3,4,5,6],
Timothy A. McKay[3,7], Leon Baruah[8], Matthew Becker[4,5,6], Christophe Benoist[9,10],
Michael Busha[4,5,6], Luiz A. N. da Costa[10,11], Jiangang Hao[12], Marcio A. G. Maia[10,11],
Christopher J. Miller[7], Ricardo Ogando[10,11], A. Kathy Romer[8], Eduardo Rozo[4,6],
Eli Rykoff[4,6], and Risa Wechsler[4,5,6]

[1]*Universitäts-Sternwarte München, Scheinerstr. 1, 81679 München, Germany*
[2]*Excellence Cluster Universe, 85748 Garching b. München, Germany*
[3]*Physics Department, University of Michigan, 450 Church St, Ann Arbor, MI 48109, USA*
[4]*Kavli Institute for Particle Astrophysics and Cosmology*
[5]*Physics Department, Stanford University, Stanford, CA, 94305, USA*
[6]*SLAC National Accelerator Laboratory, Menlo Park, CA, 94025*
[7]*Astronomy Department, University of Michigan, 500 Church St, Ann Arbor, MI 48109, USA*
[8]*Department of Physics and Astronomy, University of Sussex, UK*
[9]*Observatoire de la Côte dAzur, UMR 6202 Cassiopée, BP 4229, F-06304 Nice Cedex 4, France*
[10]*Laboratório Interinstitucional de e-Astronomia - LIneA, Rua Gal. José Cristino 77, Rio de Janeiro, RJ 20921-400, Brazil*
[11]*Observatório Nacional, R. Gal. José Cristino 77, BR Rio de Janeiro, RJ 20921-400, Brazil*
[12]*Center for Particle Astrophysics, Fermi National Accelerator Laboratory, Batavia, IL 60510, USA*

ABSTRACT

Weak-lensing measurements of the averaged shear profiles of galaxy clusters binned by some proxy for cluster mass are commonly converted to cluster mass estimates under the assumption that these cluster stacks have spherical symmetry. In this paper we test whether this assumption holds for optically selected clusters binned by estimated optical richness. Using mock catalogues created from *N*-body simulations populated realistically with galaxies, we ran a suite of optical cluster finders and estimated their optical richness. We binned galaxy clusters by true cluster mass and estimated optical richness and measure the ellipticity of these stacks. We find that the processes of optical cluster selection and richness estimation are biased, leading to stacked structures that are elongated along the line-of-sight. We show that weak-lensing alone cannot measure the size of this orientation bias. Weak lensing masses of stacked optically selected clusters are overestimated by up to 3–6 per cent when clusters can be uniquely associated with haloes. This effect is large enough to lead to significant biases in the cosmological parameters derived from large surveys like the Dark Energy Survey, if not calibrated via simulations or fitted simultaneously. This bias probably also contributes to the observed discrepancy between the observed and predicted Sunyaev-Zel'dovich signal of optically-selected clusters.

Key words: galaxies: clusters: general – gravitational lensing: weak – cosmological parameters

1 INTRODUCTION

The abundance of galaxy clusters is an important and powerful probe to constrain cosmological parameters including the Dark Energy equation of state parameter w (Allen, Evrard, & Mantz 2011). Mass-observable scaling relations are typically required to translate easily obtained mass proxies such as optical or X-ray luminosity into cluster masses, which are needed for cluster cosmology experiments. These scaling relations must be calibrated via accurate cluster mass measurements.

Weak gravitational lensing is one of the primary methods to measure the masses of galaxy clusters. Weak lensing masses can be obtained in a variety of ways. For massive galaxy clusters, the weak lensing signal is strong enough to be measurable for individual

[*] Email:dietrich@usm.lmu.de

clusters. Because the cluster mass function declines exponentially with cluster mass in the mass range of interest (Press & Schechter 1974), most clusters are too small for individual mass measurements (Kruse & Schneider 1999). These are usually binned by a proxy for their mass, such as the optical luminosity or richness, to increase the signal-to-noise ratio of the gravitational shear profile (e.g., Sheldon et al. 2009). The process of averaging cluster properties in bins is commonly called "stacking". The masses of these stacked clusters are inferred either by inverting their observed surface mass density distribution to three-dimensional density distributions under the assumption of spherical symmetry (Johnston et al. 2007a) or by fitting spherical NFW profiles (Navarro, Frenk, & White 1997) taking miscentring and the halo-halo correlation – among other components – into account (Johnston et al. 2007b).

While individual haloes are triaxial, a stacked halo profile should be spherically symmetric as long as no orientation bias enters the selection process. Such an unbiased halo selection, however, is likely impossible for optical cluster finders. Any optical identification of galaxy clusters relies on finding a significant, i.e., above a certain threshold, density contrast with respect to the surrounding field and background population. In the simplest case this is simply looking for overdensities of galaxies on the sky (Abell 1958). The near universality of galaxy cluster density profiles (Navarro et al. 1997) and luminosity functions (Schechter 1976) can be used to enhance the contrast of objects looking like galaxy clusters with respect to the background (Postman et al. 1996). The fact that the galaxy population in clusters is dominated by early-type galaxies of very similar colour, which depends only on redshift, is often used to mitigate projection effects and provide redshift estimates of galaxy clusters (e.g., Gladders & Yee 2000; Koester et al. 2007). Alternatively, photometric redshift information can be employed to add depth information to the galaxy distribution on the sky (e.g., Milkeraitis et al. 2010). No matter how sophisticated the optical cluster finding technique is, clusters that are more compact on the sky will have a higher contrast with the background and will be easier to discover.

This bias towards objects that are compact on the sky can lead to an orientation bias in galaxy cluster selection and also bias their richness estimates. Prolate (cigar-shaped) clusters with their major axis aligned with the line-of-sight (LOS) are easier to pick out and look richer than oblate (pancake-shaped) clusters whose minor axis is aligned with the LOS. If clusters are selected with such a bias, the average cluster profile in a given richness bin will not be spherically symmetric but elongated along the LOS.

In this paper we study the effects of orientation bias on the weak lensing profiles of stacked galaxy clusters and the resulting biases in mass estimation. In Section 2 we present analytic predictions for the impact of averaged cluster ellipticity on mass estimates obtained from a spherical profile inversion. We study the magnitude of orientation bias and centring errors using mock observations described in Sect. 3.1 and a number of different optical cluster finders in Section 3.2. We discuss our findings (Section 4) and their impact on cluster cosmology measurements in Section 5.

Before proceeding we clarify our nomenclature: We call halos those collapsed objects that are found by spherical overdensity (SO), friend-of-friend algorithms, or similar halo finders, in dark matter *N*-body simulations, irrespective of their galaxy content. Galaxy clusters are objects identified in observations, for the purpose of this paper in mock optical observations, as potentially corresponding to a single collapsed dark matter halo. The mappings between haloes and galaxy clusters are neither one-to-one nor onto. Throughout this paper we use a Hubble constant of $H_0 = 70\,\mathrm{km\,s^{-1}\,Mpc^{-1}}$.

2 ELLIPTICAL HALOES

As we will be dealing with elliptical haloes throughout this paper, we first need to define how to parametrise such haloes and what we mean when we assign a mass to such an object. Different authors employed different definitions in previous works (e.g., Jing & Suto 2002; Corless & King 2007, CK07 hereinafter) and it is important to clearly distinguish them from each other, decide which definition is best used for a certain purpose, and be able to convert among them. All of these definitions are generalisations of the spherical NFW profile (Navarro et al. 1997). For example, in the convention of Corless & King (2007), who follow Jing & Suto (2002) and Oguri et al. (2003), the halo density depends on the triaxial radius,

$$R^2 = \frac{X^2}{a^2} + \frac{Y^2}{b^2} + \frac{Z^2}{c^2} \quad (a \leqslant b \leqslant c = 1)\,, \qquad (1)$$

where X, Y, Z are the Cartesian coordinates with respect to the halo centre, and the virial mass is defined as the mass inside an ellipsoid with major axis R_{200} inside which the average overdensity is $200\rho_{\mathrm{c}}$, where ρ_{c} is the critical density of the Universe. This mass is given by

$$M_{200}^{\mathrm{CK}} = \frac{800\pi}{3} ab R_{200}^3 \rho_{\mathrm{c}}\,. \qquad (2)$$

While this convention is well motivated by the ellipsoidal collapse model (Sheth, Mo, & Tormen 2001) and has been used in estimating the mass calibration bias from fitting spherical NFW models to elliptical haloes (e.g., Dietrich et al. 2009; Israel et al. 2010; Applegate et al. 2014), it is probably not ideal for our purposes. We want to understand the impact of orientation bias on cosmological parameter estimates from large surveys. As many recent cluster cosmological analyses rely on the spherical overdensity mass function of Tinker et al. (2008), we should cast the impact of orientation bias in terms of the same mass convention.

We expect that no cluster finder will have a preferred angular direction on the sky. The stacked cluster profile should therefore be azimuthally symmetric around the LOS, which we take to be the z-axis of a cylindrical coordinate system (r, θ, z). We can then turn a spherical cluster profile into a biaxial elliptical profile with two even and one "odd" axis by defining an elliptical radius

$$\xi^2 = q^2 r^2 + z^2\,, \quad q > 0\,, \qquad (3)$$

where q is the ratio between the ellipsoid axis along the LOS and the other axes. This definition differs subtly from eq. (1) and the way an ellipsoid is usually defined in that q can be greater than 1. While uncommon, this choice has notational advantages later on. It is also easier to visualise the transformation of an oblate ellipsoid over a sphere to a prolate ellipsoid as a continuous stretching along the LOS. In the parametrisation of eq. (1) an oblate ellipsoid has $q = a < 1, b = c = 1$ and a prolate ellipsoid has $q = 1/a = 1/b > 1, c = 1$. Adopting the convention of CK07 would lead to awkward case distinctions later on and requires a rotation of the coordinate system if one wants the two even axes of a biaxial ellipsoid to be always in the plane of the sky. In our choice of the definition of the elliptical radius, the mass definition corresponding to eq. (2) is

$$M_{200}^{\mathrm{ell}} = \frac{800\pi}{3} q^{-2} \xi_{200}^3 \rho_{\mathrm{crit}}\,. \qquad (4)$$

We can find the spherical overdensity mass M_{200}^{SO} by numerically solving

$$\frac{3}{4\pi R_{200}^3} \int_0^{R_{200}} \int_0^\pi \int_0^{2\pi} \mathrm{d}\phi\,\mathrm{d}\theta\,\mathrm{d}r\, r^2 \sin(\theta)\rho(\xi) = 200\rho_{\mathrm{crit}} \qquad (5)$$
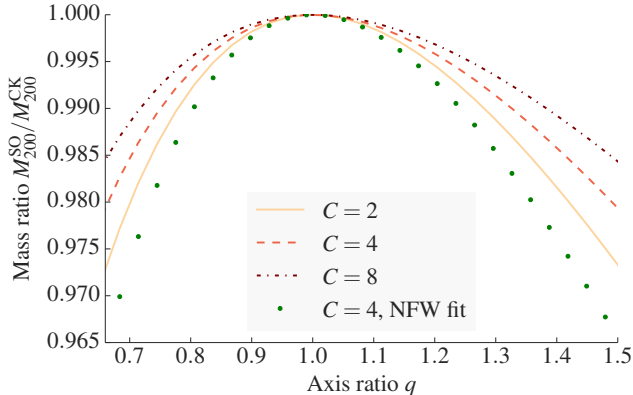
Figure 1. Conversion between the mass definition of CK07 and the spherical overdensity mass for different NFW concentrations as a function of axis ratio q. Also shown is the fit of a spherical NFW profile to the average density on spherical shells.
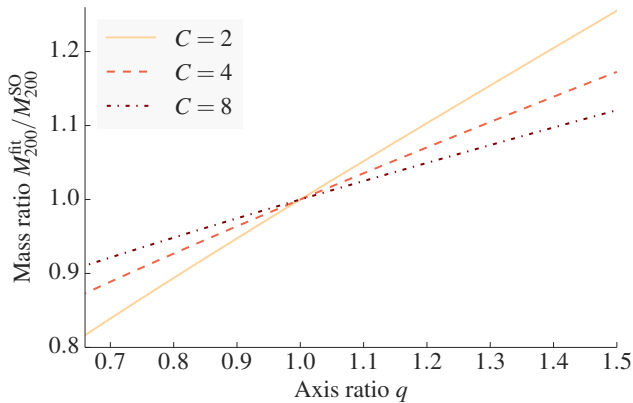

Figure 2. The ratio of best fitting M_{200} of a spherical NFW halo to the true spherical overdensity mass of an elliptical NFW halo. Different curves correspond to different concentration parameters.

for R_{200}. In Fig. 1 we show the ratio of SO masses to CK07 masses for three different NFW concentration parameters. These two mass definitions agree within 1%–2% for a wide range of realistic axis ratios (Kasun & Evrard 2005). In the same figure we also show the mass ratio for the best fit spherical NFW profile. Following the procedure outlined by CK07, we fitted a spherical NFW with free concentration and r_{200} to the average density on spherical shells. The result we find differs significantly from that reported by CK07, who find differences of up to $\sim 30\%$ between this NFW mass the CK07 mass for the axis ratios studied here. We are thus not able to reproduce the result CK07 present in their appendix but emphasise that – using their mass definition – we reproduce their predictions of the mass bias incurred when elliptical haloes are fitted under the assumption of sphericity.[1] Although our mass definition is very close to the one of CK07, we show the mass bias of fitting spherical NFW haloes to elliptical profiles in Fig. 2 for completeness and later reference.

---

[1] The conversion between SO and CK07 masses based on fitting isodensity shells to an NFW profile was not used anywhere else in CK07 and – as far as we can tell – also not in any papers citing CK07.

2.1 Spherical Inversion

CK07 studied the impact of halo ellipticity on the mass estimates obtained by fitting spherical NFW haloes to the observed reduced shear. An alternative way to obtain cluster mass estimates is the spherical inversion of the projected mass inside a cylinder using the Abel transform (Abel 1826), such as described by Johnston et al. (2007a):

$$\rho^{\text{inv}}(r) = \frac{1}{\pi} \int_r^\infty \frac{-\Sigma'(R)}{\sqrt{R^2 - r^2}} \mathrm{d}R \, , \tag{6}$$

where the prime denotes a derivative with respect to the radial coordinate.

The surface mass density Σ of any halo is obtained by integrating the 3-dimensional density profile along the LOS,

$$\begin{aligned} \Sigma^{\text{ell}}(r) &= 2 \int_0^\infty \rho[\xi(r,\theta,z)]\mathrm{d}z \\ &= 2 \int_{qr}^\infty \rho(\xi) \frac{\xi}{\sqrt{\xi^2 - q^2 r^2}} \mathrm{d}\xi \end{aligned} \tag{7}$$

Recalling that for a spherical profile (the inversion of eq. (6))

$$\Sigma^{\text{sph}}(r) = 2 \int_r^\infty \rho(R) \frac{R}{\sqrt{R^2 - r^2}} \mathrm{d}R \, , \tag{8}$$

we see that

$$\Sigma^{\text{ell}}(r) = \Sigma^{\text{sph}}(qr) \, . \tag{9}$$

This means that there is an analytical degeneracy between the surface mass density of spherical density profile and the surface mass density of an elliptical density profile with its odd axis aligned with the LOS. The two can be transformed into each other by a simple rescaling. Consequentially weak lensing alone, or any other method which depends linearly on the density, is unable to recover 3-dimensional mass information. For example, an elliptical NFW profile is exactly degenerate with a spherical NFW profile of different mass and concentration. Although this result is very straightforward to derive, it seems to us that it is not widely known. Recently Gao et al. (2012) reported their finding that the projected density profile shapes seem to be independent from the underlying 3-dimensional density distribution in a numerical study of massive galaxy clusters. This is easily explained by the degeneracy we just described.

With this degeneracy, the inversion in eq. (6) of an elliptical profile then of course recovers a rescaled spherical profile. As an illustration we consider the generalised NFW (gNFW) profile

$$\rho_{\text{gNFW}}(r; r_s) = \frac{\delta_c \rho_c}{(r/r_s)^\alpha (1 + r/r_s)^\beta} \, , \tag{10}$$

with scale radius r_s. The standard NFW profile is recovered for $(\alpha, \beta) = (1, 2)$ and a singular isothermal sphere is obtained from $(\alpha, \beta) = (2, 0)$. We show in Appendix A that if an elliptical radius ξ is used in eq. (10) instead of the spherical radius r, the Abel inversion leads to a density profile of

$$\rho_{\text{gNFW}}^{\text{inv}}(r; q, r_s) = q\rho_{\text{gNFW}}(r; r_s/q) \, . \tag{11}$$

3 METHODS

Before we proceed to measure the ellipticity introduced into stacks of optical selected clusters as a consequence of cluster finding orientation bias and richness estimation orientation bias, we describe our data sets and methods. Since knowledge of the true halo ellipticity is required to quantify the size of the orientation bias, we must work

on simulations where this information is readily available. These simulations must be realistic enough to run optical cluster finders on them and get results that resemble reality. We describe such a set of simulations as well as a suite of cluster finders applied to them in following subsections before defining how we measure the ellipticity of haloes and clusters.

3.1   Simulations

For this study we have used the mock galaxy catalogues created for the Dark Energy Survey based on the algorithm Adding Density Determined GAlaxies to Lightcone Simulations (ADDGALS; Wechsler et al. in prep.; Busha et al., in prep.). These are the same catalogs used by Szepietowski et al. (2014). We reproduce our description of these simulations from that paper in the following for the convenience of the reader.

The ADDGALS algorithm attaches synthetic galaxies, including multiband photometry, to dark matter particles in a lightcone output from a dark matter *N*-body simulation and is designed to match the luminosities, colours, and clustering properties of galaxies. The catalogue used here was based on a single Carmen simulation run as part of the LasDamas of simulations (McBride et al, in preparation)[2]. This simulation modeled a flat ΛCDM universe with $\Omega_m = 0.25$ and $\sigma_8 = 0.8$ in a 1 Gpc/*h* box with 11203 particles. A 220 sq deg light cone extending out to $z = 1.33$ was created by pasting together 40 snapshot outputs. The galaxy population for this mock catalogue was created by first using an input luminosity function to generate a list of galaxies, and then adding the galaxies to the dark matter simulation using an empirically measured relationship between a galaxy's magnitude, redshift, and local dark matter density, $P(\delta_{\rm dm}|M_{\rm r},z)$ the probability that a galaxy with magnitude $M_{\rm r}$ and redshift z resides in a region with local density $\delta_{\rm dm}$. This relation was tuned using a high resolution simulation combined with the SubHalo Abundance Matching technique that has been shown to reproduce the observed galaxy 2-point function to high accuracy (Kravtsov et al. 2004; Conroy et al. 2006; Reddick et al. 2013).

For the galaxy assignment algorithm, a luminosity function that is similar to the SDSS luminosity function as measured in Blanton et al. (2003) is chosen, but evolved in such a way as to reproduce the higher redshift observations (e.g., SDSS-Stripe 82, AGES, GAMA, NDWFS and DEEP2). In particular, ϕ^* and M are varied as a function of redshift in accordance with the recent results from GAMA (Loveday et al. 2012). Once the galaxy positions have been assigned, photometric properties are added. Here, a training set of spectroscopic galaxies taken from SDSS DR5 was used. For each galaxy in both the training set and simulation Δ_5, the distance to the 5th nearest galaxy on the sky in a redshift bin, is measured. Each simulated galaxy is then assigned a spectral energy distribution based on drawing a random training-set galaxy with the appropriate magnitude and local density, k-correcting to the appropriate redshift, and projecting onto the desired filters. When doing the colour assignment, the likelihood of assigning a red or a blue galaxy is smoothly varied as a function of redshift in order to simultaneously reproduce the observed red fraction at low and high redshifts as observed in SDSS and DEEP2. Haloes in the simulation are identified by the ROCKSTAR phase-space halo finder (Behroozi, Wechsler, & Wu 2013).

Photometric noise and error estimates are added to the

galaxy catalogue based on the depth expected for the Dark Energy Survey[3] (DES), corresponding to 5σ detection limits of $\{26.0, 25.5, 24.8, 24.3, 22.5\}$ mag in grizY bands, respectively. This results in a total number of about 21 million galaxies extending out to redshift 1.35.

3.2   Cluster Finders

A plethora of galaxy cluster finders has been developed since the proposal of Postman et al. (1996) to use a spatial matched filter algorithm on single passband data. Improvements in methodology have come primarily from the inclusion of multi-band photometry (e.g. Gladders & Yee 2000), which can either be used as a multi-dimensional colour-space in which to identify overdensities (e.g. Miller et al. 2005) or for estimating photometric redshifts (e.g. Milkeraitis et al. 2010). Improvements to the spatial filtering have also been proposed, often in the form of Voronoi tessellations (e.g. Kim et al. 2002; Soares-Santos et al. 2011).

We ran a total of four different cluster finders on the mock catalogues generated as described in the previous section. The aim here is to roughly cover the available space of modern cluster finder methods and study whether different algorithms have different orientation biases when finding galaxy clusters. We briefly describe each cluster finder below. For all clusters found with these different methods an estimate of their optical richness was computed using the λ richness estimator of Rykoff et al. (2012).

3.2.1   REDMAPPER

REDMAPPER (Rykoff et al. 2014) is a photometric cluster algorithm that identifies galaxy clusters as over-densities of red-sequence galaxies. The algorithm is divided into two stages: a calibration stage and a cluster-finding stage. In the calibration phase, redMaPPer empirically determines the colour distribution (mean and scatter) of red-sequence galaxies as a function of redshift and magnitude. This is achieved with an iterative procedure: using an a-priori red-sequence model, seed galaxies with spectroscopic redshifts in clusters are grouped with nearby potential cluster members based on colour, which are then used to calibrate the red-sequence. This model is used to re-estimate membership for every galaxy, and the red-sequence model is then re-estimated. The procedure is iterated until convergence. Once calibration is achieved, cluster finding is performed. All galaxies are considered candidate cluster centers, and assigned a redshift using our red-sequence model. Using this redshift, cluster members are found, and a new cluster redshift is estimated by simultaneously fitting the cluster members. The procedure is iterated until convergence, and then the cluster is recentered on the best possible central galaxy. The list of clusters is then rank-ordered and, in an iterative process called *percolation*, galaxies are probabilistically assigned to clusters to ensure that no cluster is counted multiple times.

3.2.2   GMBCG

Galaxy clusters almost always contain a brightest cluster galaxy (BCG) at their centers and their member galaxies tend to cluster tightly in the color space. The GMBCG cluster (Hao et al. 2010) finder utilizes these two features to find galaxy clusters.

Starting from a galaxy catalog, GMBCG first searches for BCG

---

[2] Further details regarding the simulations can be found at `http://lss.phy.vanderbilt.edu/lasdamas/simulations.html`

[3] `http://www.darkenergysurvey.org/`

candidates by applying a user-adjustable luminosity and color cut, and then tries to model the color distribution of galaxies surrounding a BCG candidate with a Error Corrected Gaussian Mixture Model (Hao et al. 2009). If the final model contains a very narrow red Gaussian component that corresponds to cluster red sequence galaxies, as well as a wider and bluer Gaussian component that corresponds to projected foreground/background galaxies and cluster "blue cloud" galaxies, GMBCG will claim to have found a cluster candidate, and counts the galaxies falling into the red sequence gaussian component as the candidate's member galaxies. Finally, gmBCG ranks all the cluster candidates by their member galaxy number counts and purges candidates according to their members' spatial distribution and whether or not they can be included in a more massive nearby cluster.

3.2.3 C4

The C4 algorithm identifies galaxies that exist in significant colour overdensities (compared to a model colour-volume density generated from random locations within the survey), and then groups them into clusters. It does so without making assumptions about the combined colour distribution of galaxy populations within clusters. The original C4 algorithm relied on complete spectroscopic redshift information (Miller et al. 2005). The version used herein has been adapted to surveys where only photometric redshift information is available (Baruah et al. in prep). Distances out to the 6th nearest neighbour are calculated in the celestial sphere for each C4 galaxy. Treating these distances as an inverse proxy for density, they are used to define the candidate cluster centres. Iterating through the candidate centre list, C4 galaxies are associated to a candidate centre (become cluster members) if they (i) lie within a 50 Mpc bin along the line of sight, and (ii) the surface-number density of the cluster exceeds some threshold above the surface density of C4 galaxies in this redshift bin. The central regions for these clusters are then defined by a radius that envelopes 25% of each cluster's membership. The cluster candidates are then merged if the central galaxy of a C4 cluster candidate can be found in the central region of a larger C4 cluster candidate, and if centres are within $\pm 0.06(1+z)$ of one another. These clusters form the C4 cluster catalog and are ranked in order of the local number density (calculated with the inverse 6th neighbour distance, as above) of the central C4 cluster galaxy.

3.2.4 WAZP

WAZP (Wavelet Adapted z Photometric, Benoist et al., in prep.) is an optical cluster finder based on the identification of galaxy overdensities in (right ascension, declination, photometric redshift z_{phot}) space. The underlying algorithm uses 2-d (right ascension, declination) and 1-d (z_{phot}) density field reconstruction based on the wavelet transform following the method proposed by Fadda, Slezak, & Bijaoui (1998). The main steps of the algorithm can be described as follows:

(i) The galaxy catalogue is sliced along the photometric redshift axis in overlapping redshift bins of variable sizes in order to follow the evolution of the photometric redshift dispersion with redshift. In each slice galaxies are selected in some magnitude range around the expected $m^*(z)$, the characteristic magnitude of a cluster luminosity function (a Schechter function) at a redshift z.

(ii) Galaxies from each slice are used to reconstruct the projected galaxy density field based on a wavelet transform method. In this reconstruction, only scales likely corresponding to clusters are kept, by default between ~ 0.5–3 Mpc.

(iii) In each slice, peaks of the density field are extracted with SExtractor configured to run without any background and with an absolute threshold set to some galaxy number density per Mpc^2.

(iv) As clusters may propagate across several slices, peaks from consecutive slices are associated, leading to the construction of cylinders (right ascension, declination, $z_{phot-min} - z_{phot-max}$), defining volumes potentially containing one or several clusters.

(v) For each cylinder the 1-d density field along the photometric redshift axis is computed based again on a wavelet transform method. One or several photometric redshift peaks are identified leading to a refinement in position and size of the clusters.

3.3 Ellipticity Measurement

A number of ways exist to measure the ellipticity of dark matter haloes[4], e.g., see Bett (2012) for a concise review of methods based on the inertia tensor. We chose to use the iterative reduced inertia tensor in this work. Briefly, we compute the reduced tensor of the mass quadrupole moments

$$\mathcal{M}_{ij} = \sum_{p=1}^{N} m_p \frac{r_{p,i} r_{p,j}}{r_p^2} , \qquad (12)$$

for a halo with N particles of mass m_p at positions $r_p = (r_{p,1}, r_{p,2}, r_{p,3})^t$ with respect to the halo centre. The eigenvalues of this tensor are the squares of the axis lengths (a, b, c) of an ellipsoid with the same mass quadrupole moments as the galaxy distribution. From these the axis ratios $t = a/c$ and $u = b/c$ are computed. These define the initial elliptical radius R as in equation (1). In further iteration steps the numerator in eq. (12) is replaced with

$$\tilde{r}_p^2 = r_{p,1}^2 + \frac{r_{p,2}^2}{t^2} + \frac{r_{p,3}^2}{u^2} , \qquad (13)$$

and only particles with $\tilde{r}_p \leqslant R$ are included in the recomputation of eq. (12). This iteration is terminated when after iteration k

$$\left| 1 - \frac{t_k}{t_{k-1}} \right| < 0.01 \qquad \text{and} \qquad \left| 1 - \frac{u_k}{u_{k-1}} \right| < 0.01 . \qquad (14)$$

By construction the galaxy density in our simulation traces the Dark Matter density and we use the galaxy distribution as proxy for the Dark Matter distribution. Instead of using the location of Dark Matter particles in the N-body simulation, we employ the position of galaxies in eqs. (12) and (13) and $m_p = 1$. As we average many haloes the sampling noise introduced by using galaxies instead of the much more numerous Dark Matter particles is negligible and our problem becomes computationally much more manageable.

For every halo, a central galaxy is defined and all the galaxies within a 3 Mpc sphere around the halo center are extracted. We stack these galaxies of different haloes according to binning of halo mass or optical richness, and run the above iteration on stacks of halo galaxies.

4 RESULTS

We now present the results of our ellipticity measurements of stacked clusters. In our analysis we only consider clusters that have a clear,

---

[4] In the following text we will only talk about haloes, although the discussion of the method applies equally well to galaxy clusters in simulations where the 3-d position of galaxies are known.

unique best halo match, as described as follows. These matches are described as two-way matches using proximity matching. Proximity matching operates by iterating through a list of haloes, from most to least massive, and imposing the condition that the highest ranked cluster (where each cluster ranking system is a proxy ordering for mass, as determined by the cluster finder's own mass-ranking mechanism) is matched within a redshift cylinder of $\Delta z = \pm 0.1$ and 1 Mpc radius local to the halo (halo-to-cluster matching). We chose $10^{13}\,\mathrm{M}_\odot$ as the cut-off mass for haloes in this process. Similarly, the clusters are matched to the haloes within redshift cylinders, going through the clusters from highest ranked to least highest ranked (cluster-to-halo matching). A uniqueness constraint is also applied, such that if a cluster has been matched to a halo previously, or vice versa (i.e. a match to a higher mass/ranked object has been previously made), it is no longer an eligible match for lower mass/ranked objects. Where a given cluster matches to a halo, and the same halo matches to that cluster, it is considered a unique, two-way match. This allows us to study the impact of orientation bias on cluster selection as a function of cluster mass without having to resort to observational proxies for mass, which in turn might be subject to orientation bias themselves. In all our analyses we take advantage of our knowledge of the true halo centres by stacking on those rather than on the cluster centroids identified by the cluster finders. We discuss this choice in Sect. 5.

To illustrate the reality of orientation bias when selecting galaxy clusters, we produced a stack of all clusters found by the REDMAPPER algorithm in the mock catalogues. In Figure 3 we show isodensity contours for two different cross-sections through the cluster stack. On the one hand the contours in the plane of the sky are circularly symmetric, consistent with our expectation that cluster finders do not have a preferred direction in this plane. On the other hand the isodensity contours show a clear elongation along the *z*-axis, the LOS in our choice of coordinate system. This establishes that orientation bias exists at least for some sub-population of all clusters when they are optically selected.

The average ellipticity of clusters binned by true cluster mass is shown in Fig. 4. At low masses galaxy clusters are strongly prolate with axis ratios $\gtrsim 1.5$. This elongation along the LOS decreases as the cluster mass exceeds $\log(M_{200}/\mathrm{M}_\odot) \approx 14.1$ or about $1.3 \times 10^{14}\,\mathrm{M}_\odot$. At the highest masses, the stacks of optically selected clusters are spherically symmetric. This trend is true for all of the cluster finding algorithms studied here. Figure 4 also shows the axis ratio for stacks of haloes found in the *N*-body simulations used in the mocks. As expected, these are consistent with being spherical.

We interpret this behaviour of the cluster finders as increasing difficulty in identifying galaxy clusters at decreasing masses. A $10^{15}\,\mathrm{M}_\odot$ cluster is such an obvious overdensity that any cluster finder will see it, regardless of its orientation. At lower masses, finding galaxy clusters becomes more of a challenge and the mechanism of orientation bias as described earlier in this paper becomes effective. It is worth pointing out that this difficulty in finding clusters depends on the intrinsic scatter in the mass-richness relation. For a higher scatter in optical richness at fixed mass, the probability of missing higher mass clusters increases because they may have fewer galaxies. Rykoff et al. (2012) and Rozo & Rykoff (2014) demonstrated that their λ richness estimator, which forms the basis of the REDMAPPER cluster finder, has a comparatively low scatter in mass at fixed richness, $\sigma_{\ln M|\lambda} \approx 0.2$–$0.3$, for an X-ray selected cluster sample. A similarly low scatter $\sigma_{\ln M|\lambda} \sim 0.2$ is also observed for a sample of > 200 Planck Sunyaev-Zeldovich (SZ) selected clusters (Rozo et al. 2014d). This is lower than the scatter in halo mass at fixed λ in our mock catalogues, which we find to be as high as 0.8.
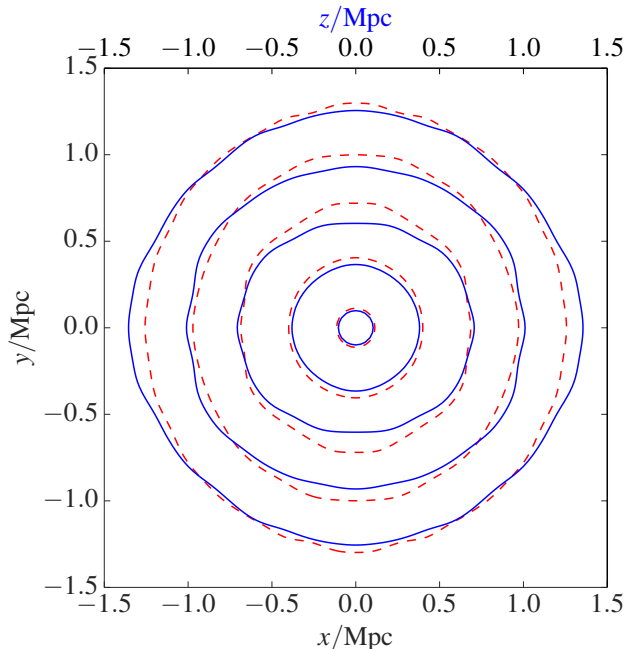

Figure 3. Isodensity contours for the stack of all REDMAPPER clusters for two different cross-sections through the stack. The clusters are stacked on the centres of the haloes to which they are matched. Red dashed contours are line of equal surface mass density in the *x-y* plane (the plane of the sky). Solid blue contours are at the same density levels in a plane perpendicular to the sky (the *y-z* plane). In this case the line-of-sight runs horizontally through the centre of the figure. To increase the signal-to-noise, these contours were generated by transforming the positions of all galaxies to the first quadrant and then reproducing that quadrant three times.
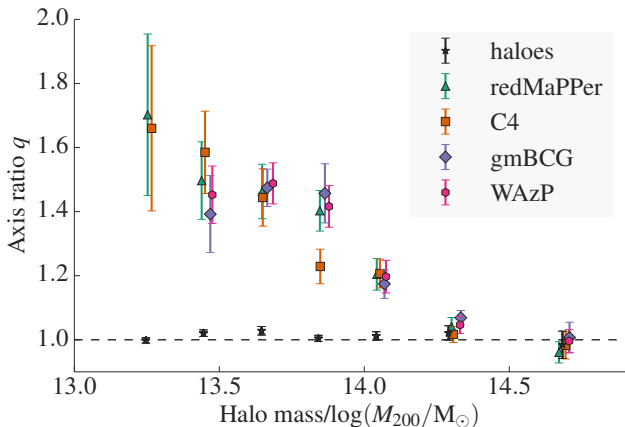

Figure 4. Measured axis ratio *q* as function of halo and cluster mass. Shown are only those clusters that could be uniquely matched to haloes. Error bars are computed from bootstrap resampling the haloes/clusters in a mass bin. Due to a minimum richness imposed by every cluster finder for inclusion in the cluster catalog fewer halos could be matched to clusters at low masses. Therefore the error bars of clusters at lower halo masses are larger than at high mass. The size of the error bars of the haloes has the opposite behaviour because more low mass haloes than high mass haloes exist and all haloes including those not matched to clusters are included in the analysis as a null test. A small intrinsic scatter between different cluster finders is present in each mass bin but the displayed points are offset in *x*-direction for clarity by an amount larger than this.
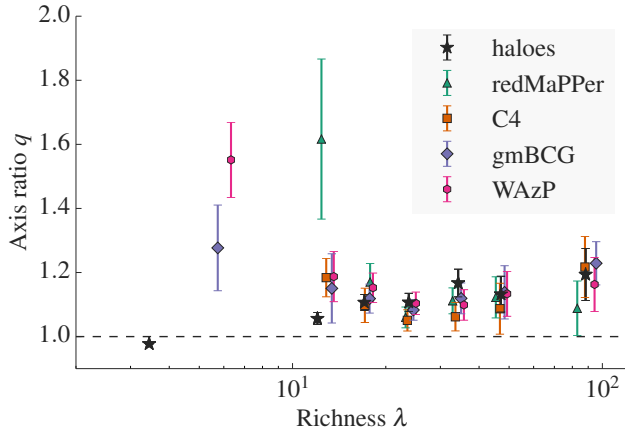
Figure 5. Measured axis ratio q as a function of estimated halo and cluster richness λ. Again horizontal offsets are applied to the data points for greater clarity.

We therefore assume that the mocks have an intrinsic scatter in the mass-richness relation that exceeds the scatter in the real Universe. The effect for our study would be that the points in Fig. 4 are shifted further to the right than they would be in real data, i.e., the effect of orientation bias would be overestimated in the mocks. In the absence of mock catalogues, which reproduce the estimated real scatter in the mass-richness relation, we tested the hypotheses that this scatter moves the location of data points in Fig. 4 from left to right with a simulation that has an even higher scatter using only the REDMAPPER cluster finder. We found that indeed the points move further to the right. It is difficult to estimate how much the curve in Fig. 4 would shift to the left if $\sigma_{\ln M|\lambda}$ is indeed as low for optically selected clusters as indicated by Rykoff et al. (2012) because many cluster finders' completeness has a complex dependency on this quantity.

In real data the true mass of clusters is of course unknown and galaxy clusters are binned by a proxy for their mass, often a richness estimator in the case of optically selected clusters. Figure 5 shows the measured axis ratio for haloes and clusters binned by the optical richness estimator λ. First, we notice that haloes, when binned by optical richness, are no longer spherical. This confirms our initial hypothesis that orientation bias is not only at work during the cluster finding process but also during richness estimation. Prolate clusters appear denser and thus richer on the sky. They are pushed to higher richness bins, which then on average deviate from spherical symmetry. This happens at the expense of the lowest richness bins, from which the prolate haloes are removed. They then appear slightly oblate at the lowest richness. The axis ratio of haloes increases with increasing λ until seemingly an approximate balance between prolate haloes that are pushed up from lower richness bins and prolate haloes that are pushed into the next higher redshift bin is established. This seems to be the case at $\lambda \gtrsim 15$. We also note that the haloes in the highest richness bin are marginally, but not significantly, more prolate than in any other bins, further supporting this scenario.

The behaviour is different for galaxy clusters. At $\lambda > 15$ the measured axis ratios for all cluster finders are consistent with being independent of richness and around $q \sim 1.1$. Significant outliers occur at lower λ for the REDMAPPER, GMBCG, and WAZP cluster finders. These values should be excluded from any interpretation of the present study. The performance of REDMAPPER is only characterised and well understood at $\lambda > 20$ (Rykoff et al. 2014), which is

the threshold adopted by the developers for inclusion of objects in the cluster catalogue. It is also important to note that REDMAPPER cluster detection and λ richness estimation are strongly intertwined and tuned to each other. Thus the two lowest richness points of the GMBCG and WAZP cluster are only presented for completeness and should not be interpreted as having reliable richness measurements and they should not be understood as an ability of these cluster finders to find lower richness clusters than REDMAPPER. Given the complex interplay between cluster selection and richness estimation, we make no attempt at an interpretation of these points.

Binning by richness as in Fig. 5 does not reproduce the trend of decreasing prolateness with increasing mass and thus increasing richness seen in Fig. 4. We observe that the scatter in optical richness leads to substantial mixing of cluster masses between richness bins. We must, however, caution that there are indications that the intrinsic scatter in the simulations exceeds that of real data and thus artificially enhances this mixing.

Furthermore, the net effect of orientation bias to push clusters into higher richness bins counteracts the decrease of axis ratios with increasing mass. The reason is that lower mass clusters, which are more subject to orientation bias in the cluster finding step and thus appear more elliptical, are preferentially measured to have higher richness as compared to the seemingly rounder high mass clusters. Thus low mass clusters are preferentially pushed into higher richness bins, resulting in a higher measured mean ellipticity. The result is that orientation bias acts as an additional correlated scatter between cluster mass and richness at fixed mass.

5 SUMMARY & DISCUSSION

We have established that optical cluster selection and richness estimation are subject to a bias heretofore unconsidered in the study of optical cluster selection. Prolate galaxy clusters are found preferentially as compared to spherical clusters, and their richness is over-estimated.

We ran a wide variety of cluster finders to test the orientation bias when selecting clusters. As a function of mass, all cluster finders studied here show a similar orientation bias. The large scatters associated with our axis ratio measurements also smear out any possible difference in the behavior of different cluster finders. A consequence of this orientation bias is that stacked weak-lensing analyses of galaxy clusters violate the previously made assumption that averaging over enough clusters makes the stacks spherically symmetric. We find instead that binning optically selected galaxy clusters by optical richness makes these stacks elliptical with axis ratios of major over minor axes $q \sim 1.1$. The exact value and its behaviour with richness likely depends on how much additional scatter the richness estimator at fixed mass has, as well as the intrinsic scatter of the mass–richness relation. The latter is larger in the simulations we used than is expected in the real Universe and the value of q we find here is an upper limit when clusters can be uniquely associated with haloes. For simplicity and because of its reported low intrinsic scatter, we have tested only the λ richness estimator (Rykoff et al. 2012). The similar orientation bias of cluster finders when rank ordered by mass turns into a similar orientation bias when clusters are rank ordered by the same richness estimator.

The choice of stacking matched clusters instead of all clusters, including false positives and clusters encompassing more than one halo, was made to avoid miscentring. Optically selected clusters have a certain rate of misidentified central galaxies, which serve as proxy for the halo centre. If we were to stack on optically identified

clusters we would incur offsets not only in the plane of the sky but also along the LOS as we know the 3-d position of galaxies and use it to to select galaxies contributing to the computation of the inertia tensor. Lensing on the other hand is not sensitive to such tiny differences in redshift and miscentring along the z-axis. Because we want to study the impact of orientation bias on lensing analyses of optically selected clusters, we chose to avoid these complications caused by miscentring by limiting the analysis to matched clusters. However, the unmatched clusters contain a certain fraction of false positives, structures that do not correspond to a cluster size halo or the superposition of two close clusters. These would typically boost the observed ellipticity and this enhanced ellipticity would also bias the lensing signal. We find that stacking all clusters indeed leads to somewhat but not significantly higher q values. We made no attempt to determine whether this difference is primarily caused by elongated structures erroneously selected as clusters, or by miscentring along the z-axis. We emphasize that these higher q values cannot be directly propagated into lensing mass biases since they are affected by miscentring along the LOS, which does not impact weak-lensing mass estimates. We did not address the question whether such a bijectively matched sub-sample of galaxy clusters used in this work could be identified in survey data when additional observables such as velocity dispersions, X-ray morphology, location on scaling relations, etc. are available. These questions can be addressed with improved simulations and future large multi-wavelength surveys.

It is well established that ellipticities in clusters lead to biases in cluster mass estimation (CK07). We find that the size of this effect for the spherical overdensity mass definition, which is the basis for the commonly used Tinker et al. (2008) cluster mass function, is very similar to that of the cluster mass definition of CK07. We emphasize that an analytical degeneracy exists for the projected density profiles of spherical haloes with elliptical haloes of a different mass and concentration. Weak lensing alone is thus unable to determine the magnitude of the orientation bias and its resultant bias in cluster mass calibration. For the axis ratios of $q \sim 1.1$ we find a mass bias of 3–6 per cent – depending on cluster concentration – is expected from Fig. 2.

Misestimation of cluster masses will contribute to inconsistencies between galaxy cluster scaling relations derived from different observables. A prominent example of such a discrepancy is the mismatch between the observed integrated Sunyaev-Zeldovich signal Y_{SZ} in early Planck data and the one predicted from cluster scaling relations (Planck Collaboration 2011). In this case, optical richness N_{200} was related to cluster mass (Johnston et al. 2007b; Rozo et al. 2009), for which in turn scaling relations for X-ray luminosity L_X and Y_{SZ} were used to predict the integrated Compton-y for given optical richnesses. The predicted values were significantly higher than the observed SZ signal. A similar effect has been observed by the Atacama Cosmology Telescope (Sehgal et al. 2013).

Orientation bias can contribute to such discrepancies. The mass of prolate cluster stacks is overestimated so that $M - N_{200}$ scaling relations predict cluster masses at a given richness that are too high. This in turn leads to higher Y_{SZ} values, as observed by the Planck Collaboration (2011). The magnitude of this affect, a rescaling of the cluster masses by 3–6 per cent, is not enough to explain this particular discrepancy fully, so that other effects like miscentring (Biesiadzinski et al. 2012) and underestimated uncertainties in the X-ray scaling relations (Rozo et al. 2014c,b) are needed in this case. Rozo et al. (2014a) showed that a self-consistent treatment of the scaling relations and proper inclusion of previously unaccounted systematic errors can resolve the tension found by the Planck Col-

laboration. As part of this process Rozo et al. (2014a) lowered their weak-lensing mass-calibration by 10 per cent, a correction they attribute to intrinsic covariance between weak lensing mass and cluster richness at fixed redshift. Orientation bias also induces such correlated scatter and although not isolated in that analysis, it is implicitly included.

A similar orientation bias is known to exist in the SZ selection of galaxy clusters (Birkinshaw et al. 1991) and has mostly been discussed in the context of measurement of the Hubble parameter using the Sunyaev-Zel'dovich effect (e.g. Jones et al. 2005). However, spatially unresolved observations – such as the Planck data – see the total integrated pressure. No additional correlation between the ellipticity of the optical MAXBCG clusters and the measured Y_{SZ} is expected from an SZ orientation bias in the (Planck Collaboration 2011) results.

Weak-lensing mass-calibration biases are propagated into cosmological parameter estimates, where scaling relations based on them are used. Assessing the bias in the determination of cosmological parameters caused by the overestimation of cluster masses due to orientation bias in previous studies is not straightforward. The additional correlated scatter caused by the orientation bias can lead to complex parameter degeneracies. This is one reason we cannot simply correct the cosmological parameters of Rozo et al. (2010) without re-running the entire MCMC. The other reason is that the their optical richness estimator is different from the λ richness estimator used in this work. We can, however, make an approximate determination of this bias by following Rozo et al. (2013): Low redshift clusters essentially constrain the quantity $s_8 = \sigma_8 \left(\Omega_m / 0.25 \right)^{\eta}$, where $\eta \approx 0.4$–0.5. Vikhlinin et al. (2009) showed that shifting the masses of all galaxy clusters in their sample by ± 9 per cent shifts the s_8 value by ± 0.024. For small shifts $\Delta \ln M_{200}$ we use a linear approximation

$$s_8 = s_{8,0} + 0.024 \frac{\Delta \ln M_{200}}{0.09} \ . \tag{15}$$

Under the assumption that the mass calibration bias is 6 per cent, the maximum value suggested by an axis ratio of $q = 1.1$, the corresponding shift in s_8 is 0.016. This is a factor two smaller than the error found by Rozo et al. (2010). Unless the MAXBCG cluster finder, for which they performed a weak-lensing cluster mass calibration, or their N_{200} richness estimator perform significantly differently from any of the cluster finders and the λ richness estimator studied here, the cosmological parameter constraints of Rozo et al. (2010) should not be significantly affected by orientation bias. Moreover, Rozo et al. (2010) considered the possibility that their lensing masses of galaxy clusters are biased by introducing a bias parameter β. Their best fit value is $\beta = 1.016 \pm 0.060$, entirely consistent with the mass bias expected from orientation bias.

Extending such forecasts to upcoming surveys like DES is not straightforward. DES is expected to find about 100 000 optically selected clusters out to a redshift $z \sim 1$. Probing the evolution of the cluster abundance with redshift helps breaking the $\Omega_m - \sigma_8$ degeneracy. Biases in mass calibration will then no longer move simply along the s_8 line. Forecasts made by Khedekar & Majumdar (2013) for DES based on a maxBCG (Koester et al. 2007) like optical cluster selection indicate that the marginalised 1σ error on Ω_m should decrease by a factor of 2.5 compared to Rozo et al. (2010) with a follow-up program obtaining cluster masses with an accuracy of 30% for only 100 clusters. Already at this level the systematic error induced by orientation bias would dominate over the statistical error. Such a limited follow-up is an extremely pessimistic assumption since there are already more clusters with observations

from the South Pole Telescope (Reichardt et al. 2013) and DES can obtain weak-lensing mass measurements via its own observations. In any case, the statistical power of surveys like the DES will be so substantial as to demand improved understanding of the effects of orientation bias.

REFERENCES

Abel N. H., 1826, Journal für die reine und angewandte Mathematik, 1, 153
Abell G. O., 1958, ApJS, 3, 211
Allen S. W., Evrard A. E., Mantz A. B., 2011, ARA&A, 49, 409
Applegate D. E. et al., 2014, MNRAS, 439, 48
Bartelmann M., 1996, A&A, 313, 697
Behroozi P. S., Wechsler R. H., Wu H.-Y., 2013, ApJ, 762, 109
Bett P., 2012, MNRAS, 420, 3303
Biesiadzinski T., McMahon J., Miller C. J., Nord B., Shaw L., 2012, ApJ, 757, 1
Birkinshaw M., Hughes J. P., Arnaud K. A., 1991, ApJ, 379, 466
Blanton M. R. et al., 2003, ApJ, 592, 819
Conroy C., Wechsler R. H., Kravtsov A. V., 2006, ApJ, 647, 201
Corless V. L., King L. J., 2007, MNRAS, 380, 149
Dietrich J. P., Biviano A., Popesso P., Zhang Y., Lombardi M., Böhringer H., 2009, A&A, 499, 669
Fadda D., Slezak E., Bijaoui A., 1998, A&AS, 127, 335
Gao L., Navarro J. F., Frenk C. S., Jenkins A., Springel V., White S. D. M., 2012, MNRAS, 425, 2169
Gladders M. D., Yee H. K. C., 2000, AJ, 120, 2148
Hao J. et al., 2009, ApJ, 702, 745
Hao J. et al., 2010, ApJS, 191, 254
Israel H. et al., 2010, A&A, 520, A58
Jing Y. P., Suto Y., 2002, ApJ, 574, 538
Johnston D. E., Sheldon E. S., Tasitsiomi A., Frieman J. A., Wechsler R. H., McKay T. A., 2007a, ApJ, 656, 27
Johnston D. E. et al., 2007b, arXiv:0709.1159
Jones M. E. et al., 2005, MNRAS, 357, 518
Kasun S. F., Evrard A. E., 2005, ApJ, 629, 781
Khedekar S., Majumdar S., 2013, J. Cosmology Astropart. Phys., 2, 30
Kim R. S. J. et al., 2002, AJ, 123, 20
Koester B. P. et al., 2007, ApJ, 660, 239
Kravtsov A. V., Berlind A. A., Wechsler R. H., Klypin A. A., Gottlöber S., Allgood B., Primack J. R., 2004, ApJ, 609, 35
Kruse G., Schneider P., 1999, MNRAS, 302, 821
Loveday J. et al., 2012, MNRAS, 420, 1239
Milkeraitis M., van Waerbeke L., Heymans C., Hildebrandt H., Dietrich J. P., Erben T., 2010, MNRAS, 406, 673
Miller C. J. et al., 2005, AJ, 130, 968
Navarro J. F., Frenk C. S., White S. D. M., 1997, ApJ, 490, 493
Oguri M., Lee J., Suto Y., 2003, ApJ, 599, 7
Planck Collaboration, 2011, A&A, 536, A12
Postman M., Lubin L. M., Gunn J. E., Oke J. B., Hoessel J. G., Schneider D. P., Christensen J. A., 1996, AJ, 111, 615
Press W. H., Schechter P., 1974, ApJ, 187, 425
Reddick R. M., Wechsler R. H., Tinker J. L., Behroozi P. S., 2013, ApJ, 771, 30
Reichardt C. L. et al., 2013, ApJ, 763, 127
Rozo E., Bartlett J. G., Evrard A. E., Rykoff E. S., 2014a, MNRAS, 438, 78
Rozo E., Evrard A. E., Rykoff E. S., Bartlett J. G., 2014b, MNRAS, 438, 62
Rozo E., Rykoff E. S., 2014, ApJ, 783, 80
Rozo E., Rykoff E. S., Bartlett J. G., Evrard A., 2014c, MNRAS, 438, 49
Rozo E., Rykoff E. S., Bartlett J. G., Evrard A. E., 2013, arXiv:1302.5086
Rozo E., Rykoff E. S., Bartlett J. G., Melin J. B., 2014d, arXiv:1401.7716
Rozo E. et al., 2009, ApJ, 699, 768
Rozo E. et al., 2010, ApJ, 708, 645
Rykoff E. S. et al., 2012, ApJ, 746, 178
Rykoff E. S. et al., 2014, ApJ, 785, 104
Schechter P., 1976, ApJ, 203, 297
Sehgal N. et al., 2013, ApJ, 767, 38
Sheldon E. S. et al., 2009, ApJ, 703, 2217
Sheth R. K., Mo H. J., Tormen G., 2001, MNRAS, 323, 1
Soares-Santos M. et al., 2011, ApJ, 727, 45
Szepietowski R. M., Bacon D. J., Dietrich J. P., Busha M., Wechsler R., Melchior P., 2014, MNRAS, 440, 2191
Tinker J., Kravtsov A. V., Klypin A., Abazajian K., Warren M., Yepes G., Gottlöber S., Holz D. E., 2008, ApJ, 688, 709
Vikhlinin A. et al., 2009, ApJ, 692, 1033
Wright C. O., Brainerd T. G., 2000, ApJ, 534, 34

APPENDIX A: ABEL INVERSION OF AN ELLIPTICAL GNFW HALO

Here we show that the spherical Abel inversion of a generalised elliptical NFW halo leads to a density profile that is described by a rescaling of the gNFW density (10) and its scale radius. The surface mass density is obtained by inserting eq. (10) into eq. (7) and using our definition of the elliptical radius $\xi^2 = q^2 r^2 + z^2$,

$$\Sigma(r;q,r_{\rm s}) = 2 \int_0^\infty {\rm d}z \frac{\delta_{\rm c}\rho_{\rm c}}{\left(\sqrt{q^2 r^2 + z^2}/r_{\rm s}\right)^\alpha \left(1 + \sqrt{q^2 r^2 + z^2}/r_{\rm s}\right)^\beta} \tag{A1}$$

For $(\alpha,\beta,q) = (1,2,1)$ this integral has been explicitly evaluated by Bartelmann (1996) and Wright & Brainerd (2000). We instead choose a different route and compute the derivative $\Sigma' = \frac{{\rm d}\Sigma}{{\rm d}r}$ of eq. (A1),

$$\Sigma'(r;q,r_{\rm s}) = -2q^2 r \int_{qr}^\infty \frac{{\rm d}\xi}{\xi\sqrt{\xi^2 - q^2 r^2}} \frac{(\alpha+\beta)\xi + \alpha r_{\rm s}}{\xi + r_{\rm s}} \rho_{\rm gNFW}(\xi;r_{\rm s}) \tag{A2}$$

The inverse Abel transform of this surface mass density profile is obtained by substituting (A2) into (6),

$$\rho_{\rm gNFW}^{\rm inv}(\xi;q,r_{\rm s}) = \frac{2}{\pi} \delta_{\rm c}\rho_{\rm c} r_{\rm s}^{\alpha+\beta} q^2 \int_\xi^\infty \frac{r\,{\rm d}r}{\sqrt{r^2 - \xi^2}} \int_{qr}^\infty \frac{{\rm d}\xi}{\xi^{\alpha+1}\sqrt{\xi^2 - q^2 r^2}} \frac{(\alpha+\beta)\xi + \alpha r_{\rm s}}{(\xi + r_{\rm s})^{(\beta+1)}} \ . \tag{A3}$$

This may be rewritten in terms of a gNFW profile using the substitutions $qu = \xi$ and $qu_{\rm s} = r_{\rm s}$,

$$\begin{aligned}\rho_{\rm gNFW}^{\rm inv}(\xi;q,r_{\rm s}) &= \frac{2q\delta_{\rm c}\rho_{\rm c} u_{\rm s}^{\alpha+\beta}}{\pi} \int_\xi^\infty \frac{r\,{\rm d}r}{\sqrt{r^2 - \xi^2}} \int_r^\infty \frac{{\rm d}u}{u^{\alpha+1}\sqrt{u^2 - r^2}} \frac{(\alpha+\beta)u + \alpha u_{\rm s}}{(u + u_{\rm s})^{\beta+1}} \\ &= \frac{2q}{\pi} \int_\xi^\infty \frac{r\,{\rm d}r}{\sqrt{r^2 - \xi^2}} \int_r^\infty \frac{{\rm d}u}{u\sqrt{u^2 - r^2}} \frac{(\alpha+\beta)u + \alpha u_{\rm s}}{u + u_{\rm s}} \rho_{\rm gNFW}(u;r_{\rm s}/q) \ .\end{aligned} \tag{A4}$$

We see now that eq. (A4) is really the expression for a spherical gNFW profile,

$$\begin{aligned}\rho_{\rm gNFW}^{\rm inv}(\xi;q,r_{\rm s}) &= \frac{-q}{\pi} \int_\xi^\infty \frac{\Sigma'(r,q=1,u_{\rm s}=r_{\rm s}/q){\rm d}r}{\sqrt{r^2 - \xi^2}} \\ &= q\rho_{\rm gNFW}(\xi;r_{\rm s}/q) \ .\end{aligned} \tag{A5}$$

This paper has been typeset from a TEX/ LATEX file prepared by the author.